Transmission compensated primary reflection retrieval in the data domain and consequences for imaging

Zhang, Lele; Thorbecke, Jan; Wapenaar, Kees; Slob, Evert

DOI
10.1190/geo2018-0340.1

Publication date
2019

Document Version
Final published version

Published in
Geophysics

GEOPHYSICS, VOL. 84, NO. 4 (JULY-AUGUST 2019); P. Q27–Q36, 17 FIGS.
10.1190/GEO2018-0340.1

Transmission compensated primary reflection retrieval in the data domain and consequences for imaging

Lele Zhang[1], Jan Thorbecke[1], Kees Wapenaar[1], and Evert Slob[1]

ABSTRACT

We have developed a scheme that retrieves primary reflections in the two-way traveltime domain by filtering the data. The data have their own filter that removes internal multiple reflections, whereas the amplitudes of the retrieved primary reflections are compensated for two-way transmission losses. Application of the filter does not require any model information. It consists of convolutions and correlations of the data with itself. A truncation in the time domain is applied after each convolution or correlation. The retrieved data set can be used as the input to construct a better velocity model than the one that would be obtained by working directly with the original data and to construct an enhanced subsurface image. Two 2D numerical examples indicate the effectiveness of the method. We have studied bandwidth limitations by analyzing the effects of a thin layer. The presence of refracted and scattered waves is a known limitation of the method, and we studied it as well. Our analysis indicates that a thin layer is treated as a more complicated reflector, and internal multiple reflections related to the thin layer are properly removed. We found that the presence of refracted and scattered waves generates artifacts in the retrieved data.

INTRODUCTION

In standard migration images, strong artifacts can occur due to internal multiple reflections in marine (Hadidi and Verschuur, 1997; Van Borselen, 2002) and land seismic data (Kelamis et al., 2006). Several schemes have been proposed to predict and subtract internal multiple reflections from measured data before the imaging procedure, such as internal multiple elimination (Berkhout and Verschuur, 2005) and inverse scattering series (ISS) (Weglein et al., 1997). Internal multiple elimination is a layer-stripping method, and it requires the identification of multiple generators in the input data. The subtraction of the predicted internal multiple reflections has to be performed by a least-squares matching filter with a minimum-energy criterion. The minimum-energy criterion can unintentionally lead to reduction or elimination of primary reflections. The ISS-based method predicts internal multiple reflections, and it reduces the effects of internal multiple reflections in the image (Weglein et al., 1997; Ten Kroode, 2002; Löer et al., 2016). A global or local matching filter is usually required to subtract the predicted internal multiple reflections from the measured data (Matson et al., 1999; Luo et al., 2011; de Melo et al., 2014).

Recently, Marchenko redatuming has been introduced to retrieve the Green's function at a virtual receiver located inside the medium for sources at the acquisition surface. This can be obtained from focusing functions and the measured reflection response at the surface (Broggini and Snieder, 2012; Wapenaar et al., 2013, 2014a). By deconvolving the retrieved upgoing Green's function with the retrieved downgoing Green's function, a virtual reflection response with virtual sources and receivers in the subsurface can be obtained. This virtual reflection response forms the basis for obtaining the artifact-free image by extracting the zero-offset and zero-time component (Broggini et al., 2014; Wapenaar et al., 2014b). It has also been shown that an artifact-free image can be obtained directly from the upgoing and downgoing parts of the focusing function (Slob et al., 2014; Wapenaar et al., 2014b). Based on Marchenko redatuming and convolutional interferometry, an internal multiple reflection elimination scheme has been proposed by Meles et al. (2015) to predict internal multiple reflections with an approximate amplitude. Except for the 1D case, these variants of Marchenko redatuming require an estimate of the first arrival of the downgoing focusing function to be able to create a virtual receiver inside the medium. This estimation requires a smooth velocity model to be built before the method can be applied. Hence, the existing methods either re-

Manuscript received by the Editor 4 May 2018; revised manuscript received 7 November 2018; published ahead of production 10 March 2019; published online 26 April 2019.
[1]Delft University of Technology, 2628 CN Delft, The Netherlands. E-mail: l.zhang-1@tudelft.nl (corresponding author); j.w.thorbecke@tudelft.nl; c.p.a.wapenaar@tudelft.nl; e.c.slob@tudelft.nl.

quire model information in the prediction and subtraction of internal multiple reflections or predict the internal multiple reflections with erroneous amplitudes.

Slob et al. (2014) show that, in a 1D medium, the unknown transmission effects can be eliminated from the initial downgoing part of the focusing function. This leads to the local reflection coefficient retrieved in the last event of the upgoing focusing function. For 3D media, van der Neut and Wapenaar (2016) and Zhang and Staring (2018) show that by projecting the focusing functions for all focusing points at a particular depth level back to a receiver location at the acquisition surface, the requirement of the estimation of the unknown initial downgoing focusing function is eliminated. In this paper, we combine the two ideas and propose to separate the internal multiple reflection elimination step from the imaging step.

The paper is organized as follows. In the "Theory" section, we start with the single-sided Green's function representations and show how the revised Marchenko equations with a new truncation operator (Zhang et al., 2018) can be derived and the initial downgoing part of the focusing function can be eliminated from the revised Marchenko equations. We then show how the last event in the upgoing part of the projected focusing function can be extracted as the primary reflection, corrected for transmission losses. We finally show how internal multiple reflections can be eliminated by filtering the data with itself. In this process, only the single-sided reflection response and the source time signature are required as input. Thus, we argue that the output of the current method is more convenient than the original data to perform velocity analysis, amplitude variation with offset analysis, and imaging.

In the numerical example section, we show two 2D examples and compare the shot gathers before and after internal multiple elimination. By comparing the amplitudes versus the traveltime of source-receiver pairs, the compensation for transmission losses is shown. The correct velocity model is used to migrate the data sets before and after internal multiple elimination using the same migration scheme in a complex subsurface model. A section about the limitations of the method investigates the effects of limited bandwidth with a thin-layer model. Refracted and scattered waves are not accounted for in the theory, and we also investigate the effects of their presence in the data.

THEORY

In this section, we derive the revised Marchenko equations from single-sided Green's function representations and project the focusing wavefield from an arbitrary depth level back to the surface, such that the process takes place entirely in the data domain. Based on these equations, we show how the transmission compensated primary reflection from the focusing depth level is present as the last event in the projected focusing wavefield. We continue by presenting the scheme of iterative internal multiple reflection elimination such that only the primary reflections with compensation for transmission effects are retained in the retrieved data set.

To develop the theory, we indicate time as t and the position vector of a spatial coordinate as $\mathbf{x} = (x, y, z)$, where z denotes the depth and (x, y) denote the horizontal coordinates. The acoustically transparent acquisition boundary $\partial\mathbf{D}_0$ is defined as $z_0 = 0$. For convenience, the coordinates at $\partial\mathbf{D}_0$ are denoted as $\mathbf{x}_0 = (\mathbf{x}_H, z_0)$, with $\mathbf{x}_H = (x, y)$. Similarly, the position vector of a point at an arbitrary depth level $\partial\mathbf{D}_i$ is denoted as $\mathbf{x}_i = (\mathbf{x}_H, z_i)$, where z_i denotes the depth of $\partial\mathbf{D}_i$. We express the acoustic impulse reflection response as $R^{\cup}(\mathbf{x}'_0, \mathbf{x}_0, t)$, where $\mathbf{x}_0$ denotes the source position and $\mathbf{x}'_0$ denotes the receiver position. In practice, it means that the free-surface-related multiple reflections should be removed from the data, and the source time signature must be known. The focusing function $f_1(\mathbf{x}_0, \mathbf{x}_i, t)$ is the solution of the homogeneous wave equation in a truncated medium and focuses at the focal point $\mathbf{x}_i$. We define the truncated medium between $z_0 < z < z_i$. Inside the truncated medium and on its boundaries, the properties of the medium are equal to the properties of the physical medium. Outside the truncated medium, the truncated medium is reflection free. The Green's function $G(\mathbf{x}_i, \mathbf{x}_0, t)$ is defined for an impulsive source that is excited at $\mathbf{x}_0$ and for a receiver positioned at the focal point $\mathbf{x}_i$. The Green's function is defined in the same medium as the measured data. The focusing and Green's functions can be partitioned into upgoing and downgoing constituents, and for this we use power-flux-normalized quantities (Wapenaar et al., 2014a).

We start with the 3D versions of one-way reciprocity theorems for flux-normalized wavefields, and we use them for the depth levels z_0 and z_i. When the medium above the acquisition level z_0 is reflection free, the Green's function can be represented as (Slob et al., 2014; Wapenaar et al., 2014a)

$$G^{-}(\mathbf{x}_i, \mathbf{x}'_0, t) = \int_{\partial\mathbf{D}_0} d\mathbf{x}_0 \int_0^{+\infty} R^{\cup}(\mathbf{x}'_0, \mathbf{x}_0, t') \times f_1^{+}(\mathbf{x}_0, \mathbf{x}_i, t - t')dt' - f_1^{-}(\mathbf{x}'_0, \mathbf{x}_i, t), \quad (1)$$

$$G^{+}(\mathbf{x}_i, \mathbf{x}'_0, -t) = -\int_{\partial\mathbf{D}_0} d\mathbf{x}_0 \int_{-\infty}^{0} R^{\cup}(\mathbf{x}'_0, \mathbf{x}_0, -t') \times f_1^{-}(\mathbf{x}_0, \mathbf{x}_i, t - t')dt' + f_1^{+}(\mathbf{x}'_0, \mathbf{x}_i, t). \quad (2)$$

Superscripts $+$ and $-$ stand for the downgoing and upgoing fields, respectively. The downgoing component of the focusing function $f_1^{+}(\mathbf{x}_0, \mathbf{x}_i, t)$ is the inverse of the transmission response in the truncated medium (Wapenaar et al., 2013). We can write the focusing function and the transmission response as the sum of a direct arrival part and a coda

$$f_1^{+}(\mathbf{x}_0, \mathbf{x}_i, t) = f_{1d}^{+}(\mathbf{x}_0, \mathbf{x}_i, t) + f_{1m}^{+}(\mathbf{x}_0, \mathbf{x}_i, t), \quad (3)$$

$$T(\mathbf{x}_i, \mathbf{x}_0, t) = T_d(\mathbf{x}_i, \mathbf{x}_0, t) + T_m(\mathbf{x}_i, \mathbf{x}_0, t), \quad (4)$$

where f_{1d}^{+} and T_d indicate the direct parts that arrive first, whereas f_{1m}^{+} and T_m indicate the following coda. The Green's and focusing functions in equations 1 and 2 are separated in time except for f_{1d}^{+} and the last event in $G^{+}(\mathbf{x}_i, \mathbf{x}'_0, -t)$ in equation 2, which coincide with each other (they have the same traveltime). We rewrite equations 1 and 2 with the help of equation 3, and this yields (Zhang et al., 2018)

$$f_1^{-}(\mathbf{x}'_0, \mathbf{x}_i, t) = \int_{\partial\mathbf{D}_0} d\mathbf{x}_0 \int_0^{+\infty} R^{\cup}(\mathbf{x}'_0, \mathbf{x}_0, t') f_1^{+}(\mathbf{x}_0, \mathbf{x}_i, t - t')dt', \quad \text{for } -t_d + \varepsilon < t < t_d + \varepsilon \quad (5)$$

$$f_{1m}^{+}(\mathbf{x}'_0,\mathbf{x}_i,t) = \int_{\partial\mathbf{D}_0} d\mathbf{x}_0 \int_{-\infty}^{0} R^{\cup}(\mathbf{x}'_0,\mathbf{x}_0,-t')f_1^{-}(\mathbf{x}_0,\mathbf{x}_i,t-t')dt', \quad \text{for } -t_d+\varepsilon < t < t_d+\varepsilon \tag{6}$$

where t_d denotes the direct one-way traveltime from a surface point $\mathbf{x}'_0$ to the focusing point $\mathbf{x}_i$ and ε is a positive value to account for the finite bandwidth in time. Note that the time truncation operator in equations 5 and 6 is asymmetric and different from the standard Marchenko scheme $(-t_d+\varepsilon < t < t_d-\varepsilon)$. As is shown in Figure 1, the f_1^- and G^- will be the same as they are in the regular case when the focusing point is far from a specific reflector. When the focusing point is close to the reflector (relative to the size of the wavelet), a choice has to be made. One should either regard the signal as belonging to f_1^- or G^-. In Slob et al. (2014) and Wapenaar et al. (2014a), the choice is made to put it in G^-, and that means that the reflection event is moved to f_1^- only when the focusing point is half a wavelength below the reflector. Here, we choose the opposite: The event is put in f_1^- as soon as the focusing point is within half a wavelength above the reflector. The fact is that this choice has to be, and can be, made due to the finite frequency bandwidth of the wavelet. Wapenaar et al. (2014b) show that

$$\int_{\partial\mathbf{D}_i} d\mathbf{x}_i \int_0^{+\infty} T_d(\mathbf{x}_i,\mathbf{x}''_0,t')f_{1d}^{+}(\mathbf{x}_0,\mathbf{x}_i,t-t')dt' = \delta(\mathbf{x}''_H-\mathbf{x}_H)\delta(t), \tag{7}$$

where $\delta(\mathbf{x}_H)$ is a spatially band-limited 2D delta function in space and $\delta(t)$ is a delta function in time. Equation 7 means that T_d is the inverse of f_{1d}^{+} in the sense that it collapses f_{1d}^{+} to a delta function in horizontal coordinates and time. Following van der Neut and Wapenaar (2016), we convolve both sides of equations 5 and 6 with T_d to find

$$v^{-}(\mathbf{x}'_0,\mathbf{x}''_0,t) = \int_{\partial\mathbf{D}_0} d\mathbf{x}_0 \int_0^{+\infty} R^{\cup}(\mathbf{x}'_0,\mathbf{x}_0,t')(\delta(t-t')\delta(\mathbf{x}''_H-\mathbf{x}_H) + v_m^{+}(\mathbf{x}_0,\mathbf{x}''_0,t-t'))dt', \quad \text{for } \varepsilon < t < t_2+\varepsilon \tag{8}$$

$$v_m^{+}(\mathbf{x}'_0,\mathbf{x}''_0,t) = \int_{\partial\mathbf{D}_0} d\mathbf{x}_0 \int_{-\infty}^{0} R^{\cup}(\mathbf{x}'_0,\mathbf{x}_0,-t')v^{-}(\mathbf{x}_0,\mathbf{x}''_0,t-t')dt', \quad \text{for } \varepsilon < t < t_2+\varepsilon \tag{9}$$

with v^- and v_m^+ defined as

$$v^{-}(\mathbf{x}'_0,\mathbf{x}''_0,t) = \int_{\partial\mathbf{D}_i} d\mathbf{x}_i \int_0^{+\infty} T_d(\mathbf{x}_i,\mathbf{x}''_0,t')f_1^{-}(\mathbf{x}'_0,\mathbf{x}_i,t-t')dt', \tag{10}$$

$$v_m^{+}(\mathbf{x}'_0,\mathbf{x}''_0,t) = \int_{\partial\mathbf{D}_i} d\mathbf{x}_i \int_0^{+\infty} T_d(\mathbf{x}_i,\mathbf{x}''_0,t')f_{1m}^{+}(\mathbf{x}'_0,\mathbf{x}_i,t-t')dt', \tag{11}$$

where t_2 denotes the two-way traveltime from a surface point $\mathbf{x}'_0$ to the focusing level z_i and back to the surface point $\mathbf{x}''_0$. Note that with this step, the requirement of the estimation of the initial downgoing focusing function has been removed because f_{1d}^{+} has collapsed to a delta function after convolution with T_d. The physical explanation of v^- can be given as follows.

Wapenaar et al. (2014b) give the relationship between two types of focusing functions as

$$f_1^{+}(\mathbf{x}'_0,\mathbf{x}_i,t) = f_2^{-}(\mathbf{x}_i,\mathbf{x}'_0,t), \tag{12}$$

$$-f_1^{-}(\mathbf{x}'_0,\mathbf{x}_i,-t) = f_2^{+}(\mathbf{x}_i,\mathbf{x}'_0,t), \tag{13}$$

where f_2 is a focusing function with its focal point at the acquisition surface. The relationship between f_2^+ and f_2^- can be given as (Wapenaar et al., 2014a)

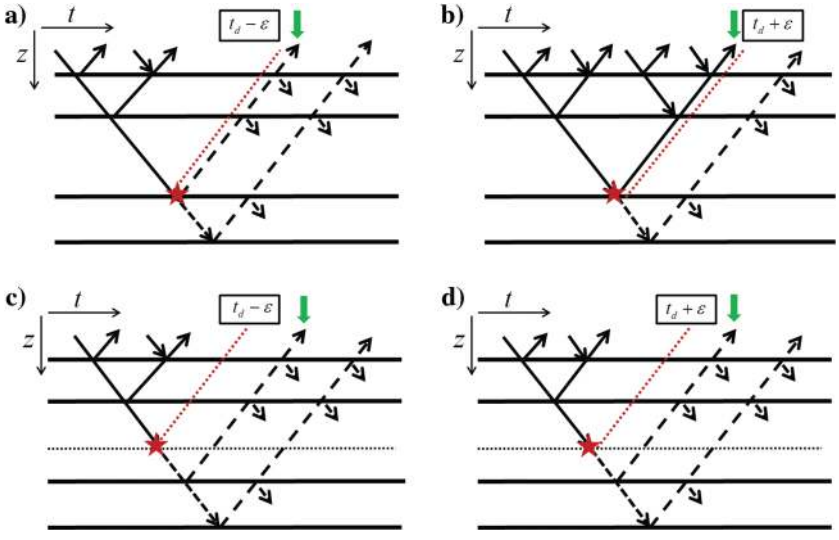

Figure 1. (a) One-dimensional sketch of f_1 and G^- in equation 1 with the focusing point just above the third reflector with the regular time truncation operator $(-t_d+\varepsilon, t_d-\varepsilon)$, (b) the f_1 and G^- in equation 1 with the revised asymmetric time truncation operator $(-t_d+\varepsilon, t_d+\varepsilon)$, (c) 1D sketch of f_1 and G^- in equation 1 with the focusing point far from the reflectors with the regular time truncation operator $(-t_d+\varepsilon, t_d-\varepsilon)$, and (d) the f_1 and G^- in equation 1 with the revised asymmetric time truncation operator $(-t_d+\varepsilon, t_d+\varepsilon)$. The dotted horizontal line in (c and d) indicates the focusing level. In each plot, the red star indicates the focusing point, the green arrow indicates the reflection event of the third reflector, the dashed red line indicates the right side of the regular or revised time truncation operator, the dashed black arrow lines indicate G^-, and the solid black arrow lines indicate f_1.

$$f_2^+(\mathbf{x}_i,\mathbf{x}'_0,t)=\int_{\partial\mathbf{D}_i}d\mathbf{x}'_i\int_0^{+\infty}R^{\cap}(\mathbf{x}_i,\mathbf{x}'_i,t'')\times f_2^-(\mathbf{x}'_i,\mathbf{x}'_0,t-t'')dt'', \tag{14}$$

where $R^{\cap}(\mathbf{x}_i,\mathbf{x}'_i,t)$ is the reflection response of the truncated medium from below, with sources and receivers at $\partial\mathbf{D}_i$. Then, we rewrite equation 10 with the help of equations 12–14 as

$$v^-(\mathbf{x}'_0,\mathbf{x}''_0,t)=-\int_{\partial\mathbf{D}_i}d\mathbf{x}_i\int_0^{+\infty}T_d(\mathbf{x}_i,\mathbf{x}''_0,t')\int_{\partial\mathbf{D}_i}d\mathbf{x}'_i\times\int_0^{+\infty}R^{\cap}(\mathbf{x}_i,\mathbf{x}'_i,t'')T^{\mathrm{inv}}(\mathbf{x}'_i,\mathbf{x}'_0,-t+t'-t'')dt''dt', \tag{15}$$

where T^{inv} is the inverse of T, and note that f_1^+ is the inverse of T as given by Wapenaar et al. (2014b). The last event in v^- is constructed by taking the first event in $R^{\cap}$ and direct event in T^{inv}; hence, the last event in v^- can be given as

$$v^-_{\mathrm{last}}(\mathbf{x}'_0,\mathbf{x}''_0,t)=-\int_{\partial\mathbf{D}_i}d\mathbf{x}_i\int_0^{+\infty}T_d(\mathbf{x}_i,\mathbf{x}''_0,t')\int_{\partial\mathbf{D}_i}d\mathbf{x}'_i\times\int_0^{+\infty}R^{\cap}_{\mathrm{first}}(\mathbf{x}_i,\mathbf{x}'_i,t'')T_d^{\mathrm{inv}}(\mathbf{x}'_i,\mathbf{x}'_0,-t+t'-t'')dt''dt', \tag{16}$$

where $R^{\cap}_{\mathrm{first}}$ indicates the first event in $R^{\cap}$, v^-_{last} indicates the last event in v^-, and T_d^{inv} indicates the direct event in T^{inv}.

Figure 2 gives the raypath of v^-_{last}. This is the reflection response with compensation for the transmission effects. Note that the amplitudes in T_d and T_d^{inv} only fully cancel each other when the medium is horizontally layered. It follows that the last event in v^- is the transmission loss compensated primary reflection of the reflector above $\partial\mathbf{D}_i$ when its two-way traveltime is t_2. Please note that the reflection coefficient contained in $R^{\cap}$ is opposite of the reflection coefficient in $R^{\cup}$, which compensates for the minus sign in equations 15 and 16. This means that v^- can be evaluated,

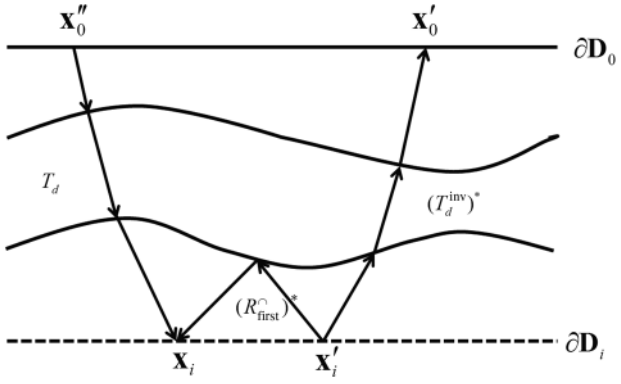

Figure 2. Raypath of v^-_{last}, (*) indicates the time-reversed version. Note that the dashed line at $\partial\mathbf{D}_i$ denotes the depth level (not a reflector) along which the integration in equation 16 takes place.

and its value at t_2 can be picked to represent a possible primary reflection event of the medium without transmission losses. Note that in the standard Marchenko scheme with symmetric time truncation, this event will be the first event without transmission effect compensation in the upgoing part of the projected Green's function (van der Neut and Wapenaar, 2016; Zhang and Staring, 2018).

Next, we give equations 8 and 9 in operator form as

$$v^-(\mathbf{x}'_0,\mathbf{x}''_0,t)=(\Theta_\varepsilon^{t_2+\varepsilon}R^{\cup}+\Theta_\varepsilon^{t_2+\varepsilon}\mathbf{R}v_m^+)(\mathbf{x}'_0,\mathbf{x}''_0,t), \tag{17}$$

$$v_m^+(\mathbf{x}'_0,\mathbf{x}''_0,t)=(\Theta_\varepsilon^{t_2+\varepsilon}\mathbf{R}^*v^-)(\mathbf{x}'_0,\mathbf{x}''_0,t), \tag{18}$$

where $\mathbf{R}$ indicates a convolution integral operator of the measured data $R^{\cup}$ with any wavefield and $\mathbf{R}^*$ is a correlation integral operator. The time window $\Theta_\varepsilon^{t_2+\varepsilon}$ excludes values outside of the interval $(\varepsilon,t_2+\varepsilon)$. We substitute equation 18 into equation 17 to get the final equation for v^- as

$$(I-\Theta_\varepsilon^{t_2+\varepsilon}\mathbf{R}\Theta_\varepsilon^{t_2+\varepsilon}\mathbf{R}^*)v^-(\mathbf{x}'_0,\mathbf{x}''_0,t)=\Theta_\varepsilon^{t_2+\varepsilon}R^{\cup}(\mathbf{x}'_0,\mathbf{x}''_0,t). \tag{19}$$

Following Van der Neut and Wapenaar (2016), we expand equation 19 as a Neumann series to give the equation as

$$v^-(\mathbf{x}'_0,\mathbf{x}''_0,t)=\Theta_\varepsilon^{t_2+\varepsilon}R^{\cup}(\mathbf{x}'_0,\mathbf{x}''_0,t)+\left[\sum_{M=1}^{\infty}(\Theta_\varepsilon^{t_2+\varepsilon}\mathbf{R}\Theta_\varepsilon^{t_2+\varepsilon}\mathbf{R}^*)^M\Theta_\varepsilon^{t_2+\varepsilon}R^{\cup}\right]\times(\mathbf{x}'_0,\mathbf{x}''_0,t). \tag{20}$$

Equation 20 is valid for each common-shot gather with a single source at $\mathbf{x}''_0$ and all receivers at $\mathbf{x}'_0$. The time window after the sum of repeated correlations and convolutions can be taken with constant values (ε and $t_2+\varepsilon$) for all traces. Because we do not have to specify the arbitrary focusing depth level z_i, the time instant t_2 can be chosen as t. We collect the value of v^- for each sampled value of t and store it in a new function containing only transmission compensated primary reflections. We can write it as

$$\bar{R}_r(\mathbf{x}'_0,\mathbf{x}''_0,t)=\bar{R}^{\cup}(\mathbf{x}'_0,\mathbf{x}''_0,t)-\bar{R}_m(\mathbf{x}'_0,\mathbf{x}''_0,t), \tag{21}$$

$$\bar{R}_m(\mathbf{x}'_0,\mathbf{x}''_0,t)=-\left[\sum_{M=1}^{\infty}(\Theta_\varepsilon^{t+\varepsilon}\mathbf{R}\Theta_\varepsilon^{t+\varepsilon}\mathbf{R}^*)^M\Theta_\varepsilon^{t+\varepsilon}\bar{R}^{\cup}\right]\times(\mathbf{x}'_0,\mathbf{x}''_0,t), \tag{22}$$

where $\bar{R}_r$ denotes the transmission compensated primary reflections and $\bar{R}_m$ is the predicted internal multiple reflections and transmission losses in the primary reflections. The bar indicates that the quantities have been convolved with the source time signature.

Equations 21 and 22 can be evaluated to obtain $\bar{R}_r$. The retrieved data set is multiple free and is more suitable for velocity model estimation and standard imaging than the original data. Moreover, we can see the operator as a mechanism to determine which parts of the data are predictable from the parts that are not. The nonpredictable parts are retained in this expression. These include the primary reflections, refracted, and scattered waves. The predictable parts are removed from this expression. These include the internal

multiple reflections and transmission effects. The processing can be performed without any model information.

EXAMPLES

In this section, two numerical examples are given to test the performance of the current scheme. In these two examples, sources and receivers are placed at the top of model with spacing of 10 m, and a Ricker wavelet, with 20 Hz center frequency, is emitted by the sources. Absorbing boundary conditions are applied around the model, and the direct wave has been removed.

Four-layer example

We give a four-layer example to test the accuracy of the proposed scheme. Figure 3 shows the values for the acoustic velocity and density of this model. We have computed the reflection responses for 401 sources and 401 receivers, and one of the computed reflection responses $\bar{R}^{\cup}(\mathbf{x}'_0, \mathbf{x}''_0, t)$ is shown in Figure 4a. Note that internal multiple reflections indicated by the red arrows are clearly present. The computed reflection responses are used as inputs to solve equations 21 and 22 for $\bar{R}_r(\mathbf{x}'_0, \mathbf{x}''_0, t)$ with $M = 1, \ldots, 20$. One of the retrieved data set is shown in Figure 4b. Internal multiple reflections visible in Figure 4a have disappeared in the retrieved data set shown in Figure 4b. The modeled primary reflections without transmission losses are shown in Figure 4c, which will be used as a reference to illustrate the success of the current scheme for internal multiple elimination and transmission losses compensation. We pick the zero-offset traces from the data sets shown in Figure 4a and 4b, and we show them in Figure 5a. It can be seen that internal multiple reflections have been successfully removed and the amplitude of the primary reflections has been changed because of the transmission compensation of the processing. A similar conclusion can be derived from Figure 5b in which the comparison of nonzero-offset traces is given. To validate the accuracy of the transmission compensation, we pick zero-offset traces from data sets shown in Figure 4b and the reference output in Figure 4c and show them in Figure 6a. It shows that the retrieved primary reflections match well with the modeled transmission-free primary reflections (quantitatively, 3%–4% error in the amplitude in the retrieved primary reflections). In Figure 6b, a comparison is made with the nonzero-offset

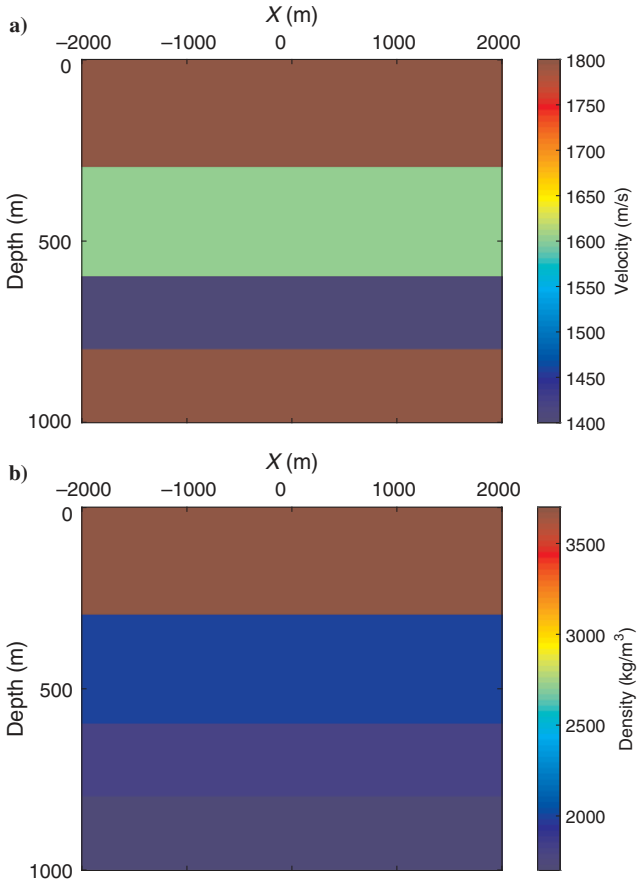

Figure 3. (a) The velocity and (b) density values of the model.

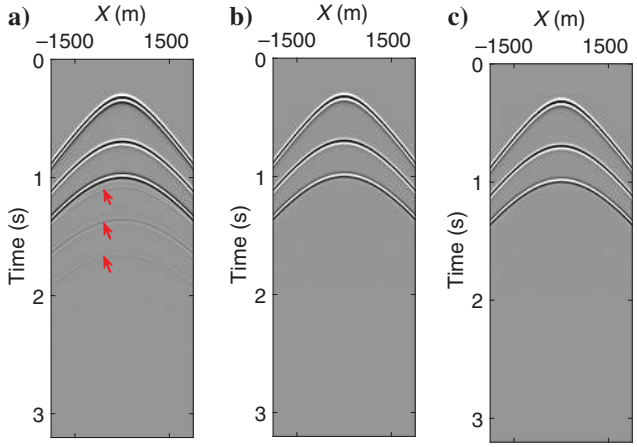

Figure 4. (a) The modeled reflection response and (b) the retrieved primary reflections using equation 21. (c) The modeled primary reflections without transmission losses. The Red arrows indicate internal multiple reflections.

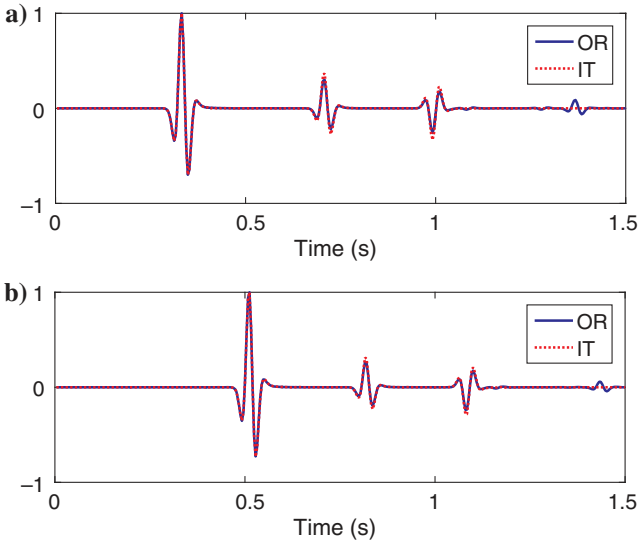

Figure 5. (a) A comparison of zero-offset traces from the original (OR) and retrieved data sets (IT) and (b) a comparison of nonzero-offset (1000 m) traces.

traces. Traces have been normalized by the same normalization factor in Figures 5 and 6. Thus, we can conclude that the current scheme can successfully remove all orders of internal multiple reflections and compensate for transmission losses in primary reflections in a horizontal layered medium.

Complex example

In this subsection, we give a 2D complex example to further test the performance of the proposed scheme. Figure 7 shows the values for the acoustic velocity and density as functions of depth and horizontal position. We have computed the reflection responses for 601 sources and 601 receivers, and one of the computed reflection responses $\bar{R}^{\cup}(\mathbf{x}'_0, \mathbf{x}''_0, t)$ is shown in Figure 8a. Note that internal multiple reflections indicated by the red arrows occur. The computed reflection responses are used as inputs to solve equations 21 and 22 for $\bar{R}_r(\mathbf{x}'_0, \mathbf{x}''_0, t)$ with $M = 1, \ldots, 20$, and the retrieved data set is shown in Figure 8b. Note that internal multiple reflections visible in Figure 8a have disappeared, whereas the later arriving primary reflections, which are seriously polluted by internal multiple reflections in Figure 8a, are clearly retrieved in Figure 8b. We pick the zero-offset traces from the data sets shown in Figure 8a and 8b, and we show them in Figure 9a. The red dotted line (IT) indicates the trace from the retrieved data set with higher amplitude because of the compensation for transmission effects. Please note that T_d and T_d^{inv} in equation 16 cannot fully cancel each other in the complex example and the transmission losses compensation is approximate. Thus, we can conclude that internal multiple reflections have been successfully removed, and transmission losses are approximately compensated after the processing in the complex example. A similar conclusion can be derived from Figure 9b in which the comparison of nonzero-offset traces is given (note that the amplitude of the first event in Figure 9b has been partly changed after the processing. This is caused by the fact that the first and second primary reflections are overlapping each other, and after the processing, the transmission losses in the second primary reflection have been approximately compensated, but the first event has not been changed). The traces in Figure 9 have been normalized by the same normalization factor. We use the original and retrieved data sets shown in Figure 8a and 8b as inputs to image the medium. At this stage, a velocity model is needed, which can, for example, be estimated from the retrieved primary reflection responses. This

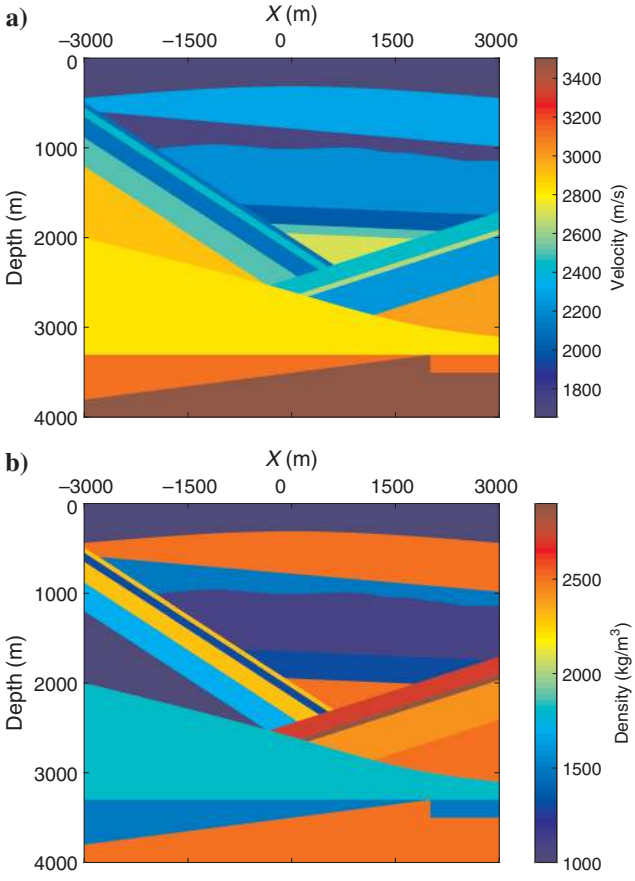

Figure 7. (a) The velocity and (b) density values of the model.

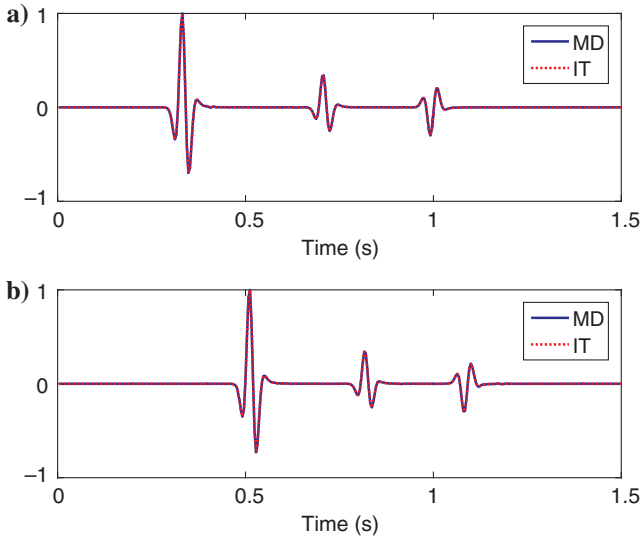

Figure 6. (a) A comparison of zero-offset traces from the modeled primary reflections (MD) and retrieved data sets (IT) and (b) a comparison of the nonzero-offset (1000 m) traces.

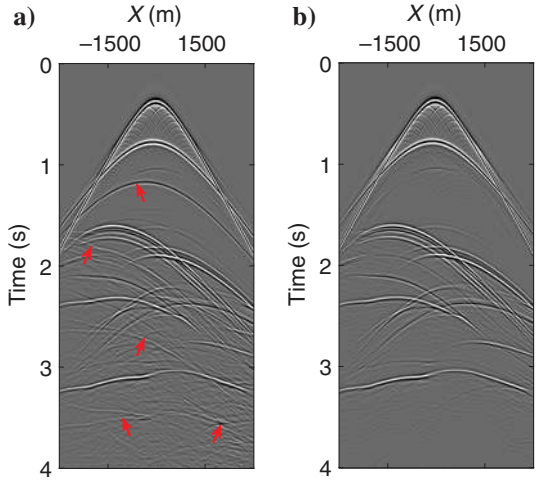

Figure 8. (a) The modeled reflection response and (b) the retrieved primary reflections using equation 21. The red arrows indicate internal multiple reflections.

retrieved data set allows much better velocity model estimation than the original data set (Dokter et al., 2017; Mildner et al., 2017) because the velocity model is built under the assumption that the data set contains only primary reflections. We use the correct velocity model for migrating both data sets. The images are shown in Figure 10a and 10b. The image in Figure 10a contains artifacts (indicated by red arrows) due to internal multiple reflections because they are imaged as if they were primary reflections. However, the image in Figure 10b, which is obtained from the retrieved data set, is excellent without ghost images due to internal multiple reflections.

LIMITATIONS ANALYSIS

In the derivation of the current method, we assumed a lossless medium. The method can be adapted to work with two-sided reflection and transmission data in dissipative media (Slob, 2016). We further assumed that the Green's functions and the focusing functions can be separated in time that the source time signature can be well-recovered, and we ignored evanescent waves (Wapenaar et al., 2013). In this section, the effect of the limited bandwidth is analyzed with a thin-layer model. We also investigate the effects of refracted and scattered waves in the data, which are not accounted for by the underlying theory. In the following examples, the source emits a Ricker wavelet with a 20 Hz center frequency and the single-sided reflection responses with 401 sources and 401 receivers with a spacing of 10 m at the top of the models have been computed. Absorbing boundary conditions are applied around the model, and the direct wave has been removed.

Thin-layer example

In this subsection, we compute numerical data in a simple horizontally layered thin-layer model to test the performance of the current scheme. Figure 11 shows the values for the acoustic velocity and density of this model. The thickness of the thin layer is 30 m (the wavelength of the source time signature at the center frequency is 90 m). One of the computed single-sided reflection responses $\bar{R}^{\cup}(\mathbf{x}'_0, \mathbf{x}''_0, t)$ is shown in Figure 12a. Note that internal multiple reflections occur in the computed response. The computed reflection responses are used as inputs to solve equations 21 and 22 for $\bar{R}_r(\mathbf{x}'_0, \mathbf{x}''_0, t)$ with $M = 1, \ldots, 20$, and one of the retrieved data set is shown in Figure 12b. The comparison of zero-offset traces from data sets shown in Figure 12a and 12b is given in Figure 13. Please note that the mismatch happens in Figure 13. In the "Discussion" section, we will analyze this mismatch in more detail.

Refracted wave example

In this subsection, we compute numerical data in a horizontally layered model with a high-velocity layer that generates refracted waves, to test the performance of the current scheme. Figure 14 shows the values for the acoustic velocity of this model (constant density 1200 kg/m^3). One of the computed single-sided reflection responses $\bar{R}^{\cup}(\mathbf{x}'_0, \mathbf{x}''_0, t)$ is shown in Figure 15a. Note that internal multiple reflections occur in the computed response and the red arrows indicate the refracted wave. The computed reflection responses are used as inputs to solve equations 21 and 22 for $\bar{R}_r(\mathbf{x}'_0, \mathbf{x}''_0, t)$ with $M = 1, \ldots, 20$, and the retrieved data set is shown in Figure 15b. Note that internal multiple reflections visible in Figure 15a have disappeared, whereas the refracted wave has been well-preserved, and new events (artifacts), which are not present in Figure 15a, have clearly appeared in Figure 15b. The

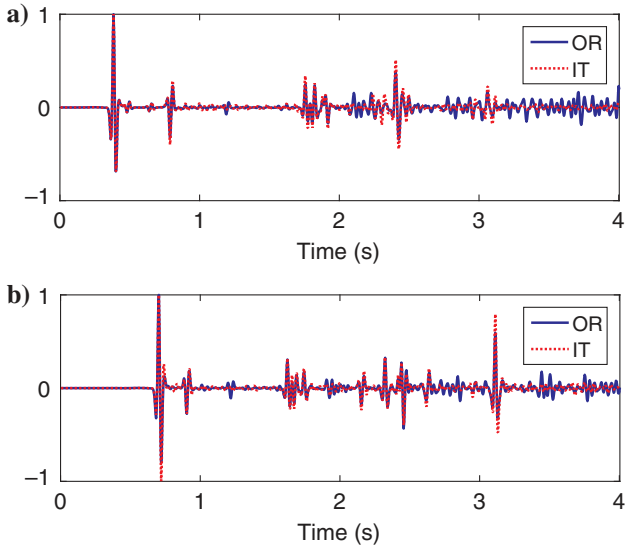

Figure 9. (a) A comparison of zero-offset traces from the original (OR) and retrieved data sets (IT) and (b) a comparison of the nonzero-offset (1000 m) traces.

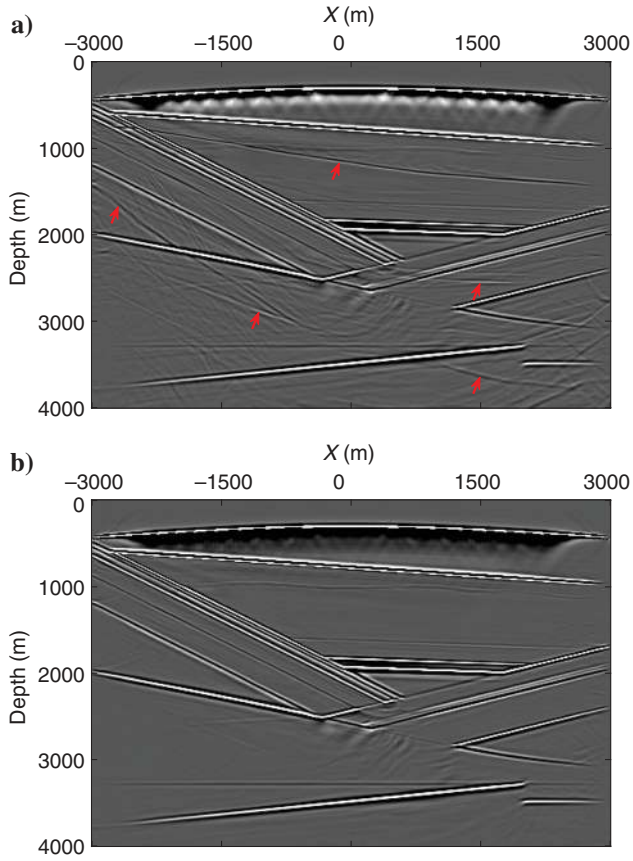

Figure 10. (a) Image of the modeled reflection responses and (b) image of the retrieved data sets. The red arrows indicate artifacts due to internal multiple reflections.

scheme did not process the diffracted waves correctly and constructed ghost events.

Scattered wave example

In this subsection, we compute the numerical data in a model that contains a scattering point to test the performance of the current

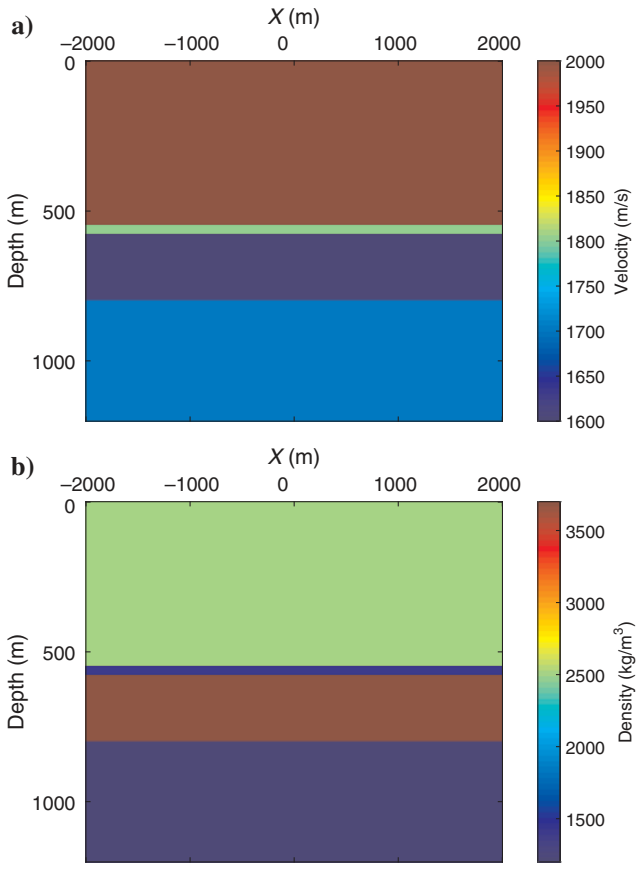

Figure 11. (a) The velocity and (b) density values of the model.

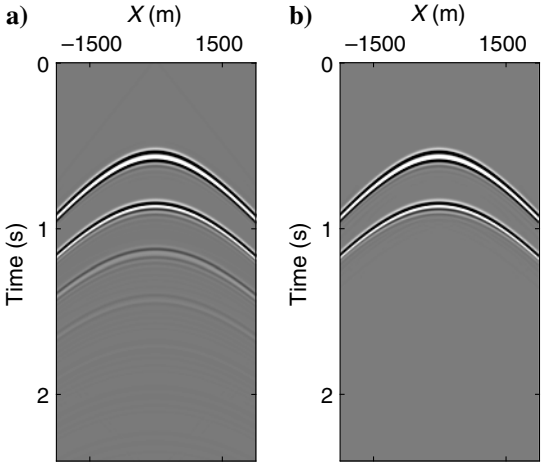

Figure 12. (a) The modeled reflection response and (b) the retrieved data set using equation 21.

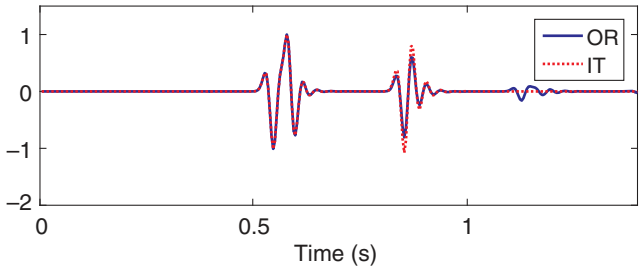

Figure 13. The comparison of zero-offset traces from the original and retrieved data sets: The solid blue line (OR) indicates the zero-offset trace from the original gather, and the red dotted line (IT) indicates the zero-offset trace from the retrieved data set (Both traces have been normalized by the same normalization factor).

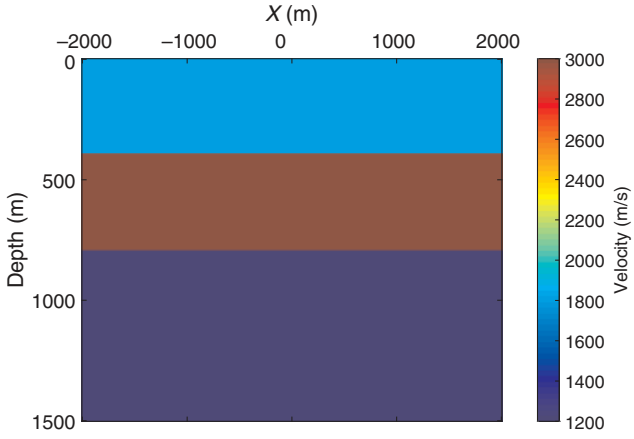

Figure 14. Velocity values of the model.

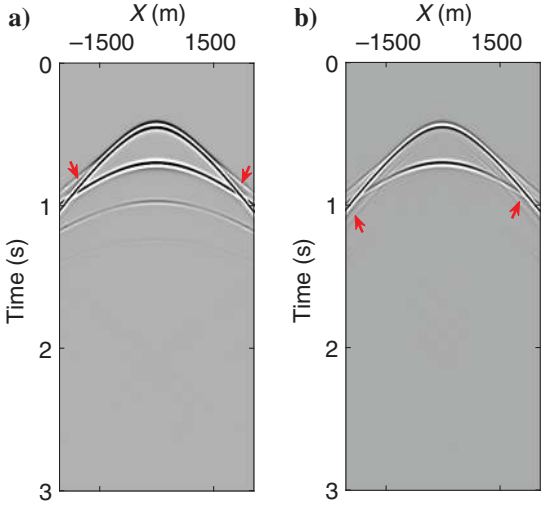

Figure 15. (a) The modeled reflection response and (b) the retrieved data set using equation 21. The red arrows in (a) indicate the refracted waves, and the red arrows in (b) indicate the generated artificial events.

scheme when scattered waves are present. Figure 16 shows the values for the acoustic velocity and density of the model. The yellow star indicates the position of the scattering point. One of the computed single-sided reflection responses $\bar{R}^{\cup}(\mathbf{x}'_0, \mathbf{x}''_0, t)$ is shown in Figure 17a. Note that scattered waves occur as indicated by the red arrows. The computed reflection responses are used as inputs to solve equations 21 and 22 for $\bar{R}_r(\mathbf{x}'_0, \mathbf{x}''_0, t)$ with $M = 1, \ldots, 20$, and the retrieved data set is shown in Figure 17b. It can be seen that the internal multiple reflection indicated by the yellow arrow in Figure 17a has been partially suppressed, whereas the multiple scattered waves are still present in Figure 17b.

DISCUSSION

In the subsection of the thin-layer example, Figure 13 shows that the thin layer is treated as a single reflector with more complicated behavior. For this reason, the primary reflection of the lower boundary in the thin layer is not touched for transmission loss compensation, and internal multiple reflections inside it are kept by the current scheme. That is why the primary reflection from the second reflector (it is the third reflector, but we observe the thin layer as a single reflector with complicated behavior) still has the imprint of the thin layer as shown in Figure 13. However, the amplitude of the primary reflection from the second reflector has been improved because of the compensation of transmission losses, and the internal multiple reflections of this reflector and the thin layer have been successfully removed. This example shows that the effect of limited bandwidth on thin-layer responses cannot be accounted for by the current scheme, but the associated internal multiple reflections between other reflectors and the thin layer are properly eliminated.

In the subsection of the refracted wave example, the refracted wave indicated by red arrows in Figure 15a is well-preserved in Figure 15b after the processing because the underlying theory of the current scheme does not account for it. The underlying theory assumes that all events are reflection events, and associated internal multiple reflections are predicted and subtracted. Unfortunately, the multiple reflections related to refracted waves do not exist in the data, and this leads to new events in Figure 15b with the same moveout as primary reflections at far offsets but that disappear at near-zero offsets. Using the event indicated by the red arrows in Figure 15b as an example, this event disappears at near zero-offsets in which the refracted wave is not present in the data, and no false multiple reflections are predicted. We observe that the presence of refracted waves in the data cannot be well accounted for during the processing, and artificial events are generated in the retrieved data set.

In the subsection of the scattered wave example, the scattered waves indicated by red arrows are preserved in Figure 17b after the processing. The internal multiple reflection indicated by the yellow arrow in Figure 17a has been partially suppressed after the processing as shown in Figure 17b. It is caused by the fact that, to totally remove the internal multiple reflection, the data should be recorded for larger offsets than used in this example.

Except for the assumptions listed in the first paragraph of the limitations analysis section, some extra limitations would affect the application of the current scheme in a field data set, such as incomplete deconvolution of the source wavelet and the presence of noise in the data set. In both cases, the predicted internal multiple reflections and transmission losses do not have the correct amplitude and phase; thus, internal multiple reflections cannot

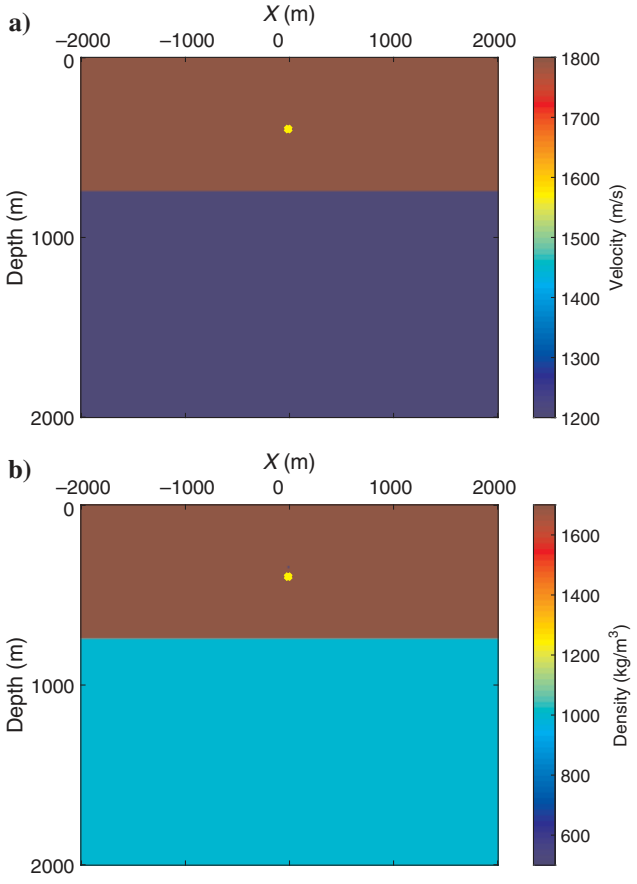

Figure 16. (a) The velocity and (b) density values of the model. The yellow stars indicate the position of the scattering point.

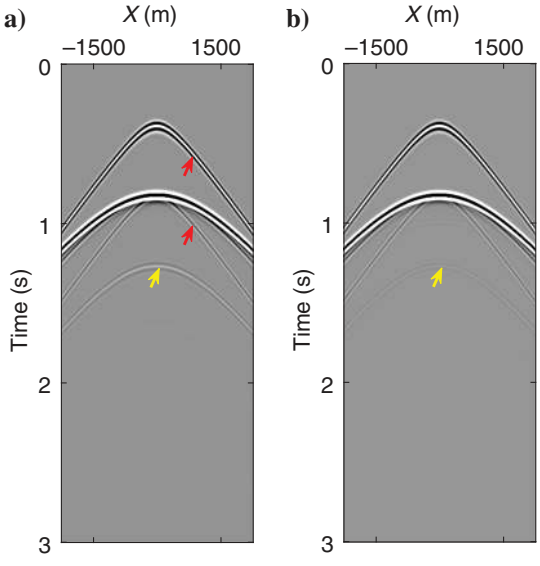

Figure 17. (a) The modeled reflection response and (b) the retrieved data set using equation 21. The red arrows indicate the scattered waves, and yellow arrows indicate the internal multiple reflections.

be completely removed and transmission losses cannot be completely compensated for.

CONCLUSION

We have shown that the single-sided reflection response can be used as its own filter to remove internal multiple reflections and to compensate for transmission losses in the primary reflections. Time windowing is applied after each convolution or correlation. No model information is required. The layered and complex numerical examples show that the method effectively removes internal multiple reflections and compensates for transmission losses. The following examples explore the limitations of the current scheme and show that scattered waves, refracted waves, and thin-layer effects are partially beyond the capability of the current method. We expect that the current method can be used in seismic reflection imaging and monitoring of structures and processes in the earth's interior. The method opens a new way to investigate how independent information about the internal structure of a medium is contained in measured acoustic data. It also allows investigating how this information can be retrieved without information of the medium and how it can be used to produce an accurate image.

ACKNOWLEDGMENTS

This work is part of the Open Technology Program with project number 13939, which is financed by NWO Domain Applied and Engineering Sciences. We would like to thank J. Etgen, I. Moore, M. Ravasi, F. Broggini, and two anonymous reviewers for their valuable suggestions. We are also grateful to J. van der Neut and M. Staring for the fruitful discussions. The research of K. Wapenaar has received funding from the European Research Council (ERC) under the European Union's Horizon 2020 research and innovation programme (grant agreement no. 742703).

DATA AND MATERIALS AVAILABILITY

Data associated with this research are available and can be obtained by contacting the corresponding author.

REFERENCES

Berkhout, A. J., and D. J. Verschuur, 2005, Removal of internal multiples with the common focus-point (CFP) approach — Part 1: Explanation of the theory: Geophysics, **70**, no. 3, V45–V60, doi: 10.1190/1.1925753.

Broggini, F., and R. Snieder, 2012, Connection of scattering principles: A visual and mathematical tour: European Journal of Physics, **33**, 593–613, doi: 10.1088/0143-0807/33/3/593.

Broggini, F., R. Snieder, and K. Wapenaar, 2014, Data-driven wave field focusing and imaging with multidimensional deconvolution: Numerical examples from reflection data with internal multiples: Geophysics, **79**, no. 3, WA107–WA115, doi: 10.1190/geo2013-0307.1.

de Melo, F. X., M. Idris, Z. J. Wu, and C. Kostov, 2014, Cascaded internal multiple attenuation with inverse scattering series: 84th Annual International Meeting, SEG, Expanded Abstracts, 4113–4117, doi: 10.1190/segam2014-0863.1.

Dokter, E., G. A. Meles, A. Curtis, and K. Wapenaar, 2017, Velocity analysis using surface-seismic primaries-only data obtained without removing multiples: 79th Annual International Conference and Exhibition, EAGE, Extended Abstracts, We-B2-03.

Hadidi, M. T., and D. J. Verschuur, 1997, Removal of internal multiples — Field data examples: 59th Annual International Conference and Exhibition, EAGE, Extended Abstracts, A013.

Kelamis, P. G., W. Zhu, K. O. Rufaii, and Y. Luo, 2006, Land multiple attenuation: The future is bright: 76th Annual International Meeting, SEG, Expanded Abstracts, 2699–2703, doi: 10.1190/1.2370082.

Löer, K., A. Curtis, and G. A. Meles, 2016, Relating source-receiver interferometry to an inverse-scattering series to derive a new method to estimate internal multiples: Geophysics, **81**, no. 3, Q27–Q40, doi: 10.1190/geo2015-0330.1.

Luo, Y., P. G. Kelamis, S. Huo, G. Sindi, S. Hsu, and A. B. Weglein, 2011, Elimination of land internal multiples based on the inverse scattering series: The Leading Edge, **30**, 884–889, doi: 10.1190/1.3626496.

Matson, K., D. Corrigan, A. Weglein, C. Young, and P. Carvalho, 1999, Inverse scattering internal multiple attenuation: Results from complex synthetic and field data examples: 89th Annual International Meeting, SEG, Expanded Abstracts, 1060–1063, doi: 10.1190/1.1820681.

Meles, G., K. Löer, M. Ravais, A. Curtis, and C. A. da Costa Filho, 2015, Internal multiple prediction and removal using Marchenko autofocusing and seismic interferometry: Geophysics, **80**, no. 1, A7–A11, doi: 10.1190/geo2014-0408.1.

Mildner, C., F. Broggini, J. O. A. Robertsson, D. Jan van Manen, and S. Greenhalgh, 2017, Target-oriented velocity analysis using Marchenko-redatumed data: Geophysics, **82**, no. 2, R75–R86, doi: 10.1190/geo2016-0280.1.

Slob, E., 2016, Green's function retrieval and Marchenko imaging in a dissipative acoustic medium: Physical Review Letters, **116**, 164301, doi: 10.1103/PhysRevLett.116.164301.

Slob, E., K. Wapenaar, F. Broggini, and R. Snieder, 2014, Seismic reflector imaging using internal multiples with Marchenko-type equations: Geophysics, **79**, no. 2, S63–S76, doi: 10.1190/geo2013-0095.1.

Ten Kroode, P. E., 2002, Prediction of internal multiples: Wave Motion, **35**, 315–338, doi: 10.1016/S0165-2125(01)00109-3.

Van Borselen, R. G., 2002, Fast-track, data-driven interbed multiple removal — A North Sea data example: 64th Annual International Conference and Exhibition, EAGE, Extended Abstracts, F-40.

van der Neut, J., and K. Wapenaar, 2016, Adaptive overburden elimination with the multidimensional Marchenko equation: Geophysics, **81**, no. 5, T265–T284, doi: 10.1190/geo2016-0024.1.

Wapenaar, K., F. Broggini, E. Slob, and R. Snieder, 2013, Three-dimensional single-sided Marchenko inverse scattering, data-driven focusing, Green's function retrieval, and their mutual relations: Physical Review Letters, **110**, 084301, doi: 10.1103/PhysRevLett.110.084301.

Wapenaar, K., J. Thorbecke, J. van der Neut, F. Broggini, E. Slob, and R. Snieder, 2014a, Green's function retrieval from reflection data, in absence of a receiver at the virtual source position: Journal of the Acoustical Society of America, **135**, 2847–2861, doi: 10.1121/1.4869083.

Wapenaar, K., J. Thorbecke, J. van der Neut, F. Broggini, E. Slob, and R. Snieder, 2014b, Marchenko imaging: Geophysics, **79**, no. 3, WA39–WA57, doi: 10.1190/geo2013-0302.1.

Weglein, A. B., F. A. Gasparotto, P. M. Carvalho, and R. H. Stolt, 1997, An inverse scattering series method for attenuating multiples in seismic reflection data: Geophysics, **62**, 1975–1989, doi: 10.1190/1.1444298.

Zhang, L., E. Slob, J. van der Neut, and K. Wapenaar, 2018, Artifact-free reverse time migration: Geophysics, **83**, no. 5, A65–A68, doi: 10.1190/geo2017-0795.1.

Zhang, L., and M. Staring, 2018, Marchenko scheme based internal multiple reflection elimination in acoustic wavefield: Journal of Applied Geophysics, **159**, 429–433, doi: 10.1016/j.jappgeo.2018.09.024.